Breather arrest, localization, and acoustic non-reciprocity in dissipative nonlinear lattices

Alireza Mojahed,[1,a)] Oleg V. Gendelman,[2] and Alexander F. Vakakis[1]
[1]*Mechanical Science and Engineering, University of Illinois, Urbana, Illinois 61801, USA*
[2]*Faculty of Mechanical Engineering, Technion, Haifa, Israel*

(Received 5 October 2018; revised 6 February 2019; accepted 6 February 2019; published online 31 July 2019)

The effect of on-site damping on breather arrest, localization, and non-reciprocity in strongly nonlinear lattices is analytically and numerically studied. Breathers are localized oscillatory wavepackets formed by nonlinearity and dispersion. Breather arrest refers to breather disintegration over a finite "penetration depth" in a dissipative lattice. First, a simplified system of two nonlinearly coupled oscillators under impulsive excitation is considered. The exact relation between the number of beats (energy exchanges between oscillators), the excitation magnitude, and the on-site damping is derived. Then, these analytical results are correlated to those of the semi-infinite extension of the simplified system, where breather penetration depth is governed by a similar law to that of the finite beats in the simplified system. Finally, motivated by the experimental results of Bunyan, Moore, Mojahed, Fronk, Leamy, Tawfick, and Vakakis [Phys. Rev. E **97**, 052211 (2018)], breather arrest, localization, and acoustic non-reciprocity in a non-symmetric, dissipative, strongly nonlinear lattice are studied. The lattice consists of repetitive cells of linearly grounded large-scale particles nonlinearly coupled to small-scale ones, and linear intra-cell coupling. Non-reciprocity in this lattice yields either energy localization or breather arrest depending on the position of excitation. The nonlinear acoustics governing non-reciprocity, and the surprising effects of existence of linear components in the coupling nonlinear stiffnesses, in the acoustics, are investigated.
© *2019 Acoustical Society of America*. https://doi.org/10.1121/1.5114915

[MRH] Pages: 826–842

I. INTRODUCTION

Discrete breathers are spatially localized oscillatory wavepackets formed due to strong nonlinear interactions between adjacent linearly grounded particles in a discrete lattice.[1] Traveling breathers are spatially localized wavepackets that travel undistorted (or nearly undistorted) through the lattice.[2–4] These special nonlinear propagating waveforms are made possible by the delicate balance between nonlinearity and dispersion, and typically incorporate two different lengths (and time) scales, namely, a slowly varying envelope enclosing a fast-varying oscillation. An example of a strongly nonlinear medium that supports traveling breathers is the homogeneous one-dimensional (1 D) ordered granular chain.[5–7] Asymptotic analysis has shown that for nonlinear lattices with weak cubic nonlinearity, the approximate equation governing the form and the slowly varying amplitude of the envelope of the breather is the discrete nonlinear Schrodinger (DNLS) equation,[8] while for the case of granular chains, the governing equation is of the form of the discrete nonlinear p-Schrodinger (DNLpS) equation.[7] A somewhat similar analysis of lattices with strong cubic nonlinearities yields analogous results for traveling breathers. Indeed, there is rich literature on the topic of traveling breathers or propagating solitons in different types of nonlinear lattices such as Toda,[9] Ablowitz–Ladik,[10] and Klein–Gordon[11–14] lattices, with analytical[4] and numerical[12–14] approaches. One property that most, if not all, of these studies have in common is that they consider Hamiltonian lattices, i.e., they omit the effects of dissipation in breather propagation. This is not surprising, given that in the presence of dissipation, e.g., viscous damping, and in the absence of a sustained external source of energy, e.g., an applied periodic force, traveling breather propagation changes from stationary to non-stationary, thus changing completely both the governing mathematical physics and the nonlinear acoustics of the problem.

In the present study, we aim to investigate and understand non-reciprocity and the effects of on-site damping on breather penetration depth in essentially nonlinear semi-infinite lattices subject to impulsive excitations at their boundaries. Preliminary numerical results associated with an impulsively excited, dissipative, semi-infinite, nonlinear lattice incorporating internal scale hierarchy and asymmetry[15] revealed that traveling breathers disintegrated after propagating through only a finite number of lattice particles; moreover, interesting non-reciprocal acoustics were detected. In the first section of this work, we initiate our investigation of the effects of dissipation on breather propagation and arrest by considering a simplified two-degree-of-freedom (2 DOF) system of two nonlinearly coupled particles grounded through linear stiffness and viscous damping. When this system is excited by an impulse, a finite number of nonlinear beats (i.e., energy exchanges) between the two particles occurs. The exact relation between the number of beats, the impulse amplitude, and the viscous damping coefficient is analytically derived. Then, a breather penetration study for

---

[a)] Electronic mail: mojahed2@illinois.edu

0001-4966/2019/146(1)/826/17/$30.00

an impulsively excited 1 D nonlinear lattice representing the semi-infinite extension of the simplified 2 DOF system is numerically performed, and the results are compared to the corresponding analytical results for the simplified 2 DOF system. Surprisingly, the results on breather penetration for the semi-infinite lattice appear to correlate closely with the finite number of beats in the simplified system. Following these studies, we numerically investigate breather penetration in a semi-infinite nonlinear asymmetric hierarchical lattice, similar to the finite lattice studied in Ref. 15 and compare the results to those of the symmetric nonlinear lattice considered earlier. Furthermore, interesting non-reciprocal acoustic phenomena are investigated. Before discussing the results on acoustic non-reciprocity, a few basic definitions regarding reciprocity in linear and nonlinear systems should be reviewed. Reciprocity is one of the fundamental properties of linear time-invariant dynamical systems. Mathematically, this feature reveals itself in the form of symmetric Green's functions and self-adjoint governing operators. According to the Onsager-Casimir principle of microscopic reversibility, reciprocity is directly related to time-reversal symmetry of the response.[16–18] Hence, to be able to break reciprocity, one must break time-reversal symmetry, and to this end one can take several different approaches; namely, implementing odd-symmetric external biases (which are likely to violate parity-time-symmetry of the lattice),[19–23] considering time-varying system parameters, or incorporating nonlinearities.[15,24–28] Here, in this paper, we aim to investigate in more detail a lattice, which was proved to exhibit acoustic non-reciprocity (both numerically and experimentally) in Ref. 15. The non-reciprocal acoustics of this specific nonlinear lattice is demonstrated by either immediate breather confinement and wave localization, or finite breather propagation and then arrest, depending on the point of application and the amplitude of the impulsive excitation. The bifurcations governing these non-reciprocal acoustics are investigated, and the nonlinear mechanisms governing these phenomena are discussed. We end by summarizing the main findings in this work.

II. SIMPLIFIED SYSTEM—BEAT ARREST

We start by considering the preliminary, simplified system shown in Fig. 1. Our aim is to study the effect of damping and input energy to the system on the energy exchanges between the two oscillators. The simplified system consists of two identical particles with mass m, grounded by pairs of linear springs and viscous dampers with constants k and d, respectively, and are coupled by means of a strongly nonlinear (in fact, non-linearizable) cubic stiffness with constant C.

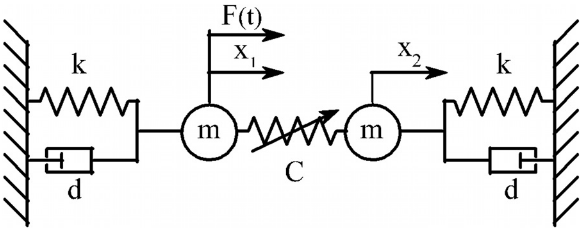

FIG. 1. Configuration of the 2 DOF nonlinear system.

The system is assumed with zero initial conditions and an impulse of intensity F_0 is applied to one of the two oscillators.

The corresponding governing equations of motion are given by

$$\begin{aligned} &m\ddot{x}_1 + kx_1 + d\dot{x}_1 + C(x_1 - x_2)^3 = F(t) = F_0\delta(t), \\ &m\ddot{x}_2 + kx_2 + d\dot{x}_2 + C(x_2 - x_1)^3 = 0, \\ &x_1(0+) = x_2(0+) = 0,\ \dot{x}_1(0+) = \dot{x}_2(0+) = 0, \end{aligned} \tag{1}$$

where $\delta(t)$ is the Dirac function. Applying the change of variables $\omega_n t = \tau,\ k = \omega_n{}^2 m,\ x_1 = \alpha u_1,\ x_2 = \alpha u_2,\ \lambda = d/(m\omega_n)$, we normalize the equations of motion as follows:

$$\begin{aligned} &u_1'' + u_1 + \lambda u_1' + (u_1 - u_2)^3 = 0, \\ &u_2'' + u_2 + \lambda u_2' + (u_2 - u_1)^3 = 0, \\ &u_1(0+) = u_2(0+) = 0, \quad u_1'(0+) = F_0/\alpha k \equiv I_0, \\ &u_2'(0+) = 0, \end{aligned} \tag{2}$$

where $\alpha = \sqrt{k/C}$, $(\cdot)' = d(\cdot)/d\tau$, and the impulse excitation term in the first equation of system (1) is replaced by an equivalent initial condition for u_1' at $\tau = 0+$. At this point we introduce two new dependent variables to describe the dynamics, one in terms of the motion of the center of mass of the system, $v = (u_1 + u_2)/2$, and the other describing the relative motion between the two particles, $w = u_1 - u_2$. Then Eq. (2) is expressed as the following system of uncoupled oscillators:

$$\begin{aligned} &v'' + v + \lambda v' = 0, \\ &w'' + w + \lambda w' + 2w^3 = 0, \\ &v(0+) = 0, \quad v'(0+) = I_0/2, \quad w(0+) = 0, \\ &w'(0+) = I_0. \end{aligned} \tag{3}$$

We note that the motion of the center of mass of the system is governed by a damped linear harmonic oscillator whose exact solution is trivial, whereas the relative displacement between the two particles is governed by a damped cubic oscillator. Unfortunately, the nonlinear differential equation governing the second expression in Eq. (3) is not solvable in terms of known (tabulated) functions[29] so can admit only an approximate solution through asymptotic methods. Indeed, for sufficiently small values of w the analytical solutions of system (3) are given by

$$\begin{aligned} &v(\tau) = \frac{I_0}{2}\exp(-\lambda\tau/2)\sin(\tau), \\ &w(\tau) \approx N_0\exp(-\lambda\tau/2)\sin\left\{\tau + \frac{3N_0^2}{4\lambda}[1 - \exp(-\lambda\tau)]\right\}, \end{aligned} \tag{4}$$

where N_0 is the only real root of $N(1 + 3N^2/4) = I_0$ according to the initial conditions in Eq. (3). Moreover, details on derivation of the response $w(\tau)$ are provided in the Appendix.

Considering the previous results, the motion of the two oscillators can be analytically approximated as

$$\begin{aligned} u_1(\tau) \approx{}& \frac{I_0 - N_0}{2}\exp(-\lambda\tau/2)\sin(\tau) \\ &+ N_0 \exp(-\lambda\tau/2)\sin\left\{\tau + \frac{3N_0^2}{8\lambda}[1-\exp(-\lambda\tau)]\right\} \\ &\times \cos\left\{\frac{3N_0^2}{8\lambda}[1-\exp(-\lambda\tau)]\right\}, \\ u_2(\tau) \approx{}& \frac{I_0 - N_0}{2}\exp(-\lambda\tau/2)\sin(\tau) \\ &- N_0 \exp(-\lambda\tau/2)\cos\left\{\tau + \frac{3N_0^2}{8\lambda}[1-\exp(-\lambda\tau)]\right\} \\ &\times \sin\left\{\frac{3N_0^2}{8\lambda}[1-\exp(-\lambda\tau)]\right\}. \end{aligned} \tag{5}$$

A first observation from the solutions (5) is that each response is composed of two terms, namely, an exponentially decaying oscillation which is common in both responses, and a second decaying but "beating" term. The beating terms incorporate two different scales in the sense that they describe "fast" oscillations of the two particles at normalized frequency close to unity with relative phase of $\pi/2$, bounded by exponentially decaying "slow" envelopes. Hence, the solutions (5) describe nonlinear beats between the two coupled oscillations, in the form of recurring energy exchanges with energy from one of the oscillators being transferred to the other and vice versa. It is interesting that, as discussed below, the number of beats is *finite* and can be analytically predicted. Indeed, for small values of I_0 (i.e., for sufficiently small applied impulses) the non-beating terms in Eq. (5) may be neglected (although this assumption is not necessary), and an analytical relation between the number of beatings n, the impulsive intensity measure I_0, and the normalized damping coefficient λ may be derived. From Eq. (5), the envelopes $U_1(\tau)$ and $U_2(\tau)$ of the beating terms for the responses $u_1(\tau)$ and $u_2(\tau)$, respectively, can be expressed as

$$\begin{aligned} U_1(\tau) &= N_0 \exp(-\lambda\tau/2)\left|\cos\left\{\frac{3N_0^2}{8\lambda}[1-\exp(-\lambda\tau)]\right\}\right|, \\ U_2(\tau) &= N_0 \exp(-\lambda\tau/2)\left|\sin\left\{\frac{3N_0^2}{8\lambda}[1-\exp(-\lambda\tau)]\right\}\right|. \end{aligned} \tag{6}$$

Figures 2(a) and 2(b) depict the analytical envelopes, $U_1(\tau)$ and $U_2(\tau)$, in comparison to the corresponding envelopes of the responses, $u_1(\tau)$ and $u_2(\tau)$, derived from direct numerical integrations of Eq. (2) for $I_0 = 0.1$ and $\lambda = 5 \times 10^{-4}$; this comparison demonstrates the accuracy of the analysis. Beating phenomena which correspond to intense recurring energy exchanges between the two oscillators are clearly detected. Moreover, we note that the number of beats, n, in the responses of $u_1(\tau)$ or $u_2(\tau)$ is directly related to the number of zeros of the envelopes $U_1(\tau)$ and $U_2(\tau)$, respectively.

Since the current study is computational, we provide some details of the numerical approach taken to solve the governing equations of motion. All ordinary differential equations are integrated using the ODE45 command of MATLAB® which is based on explicit Dormant-Prince method, a member of Runge-Kutta ODE solver family. To ensure reliable results, relative and absolute error tolerances were set to 10^{-10}. Moreover, the initial step size as well as the maximum step size in the algorithm was set equal to 1/20 of the period of oscillation corresponding to the highest linearized frequency of the system.

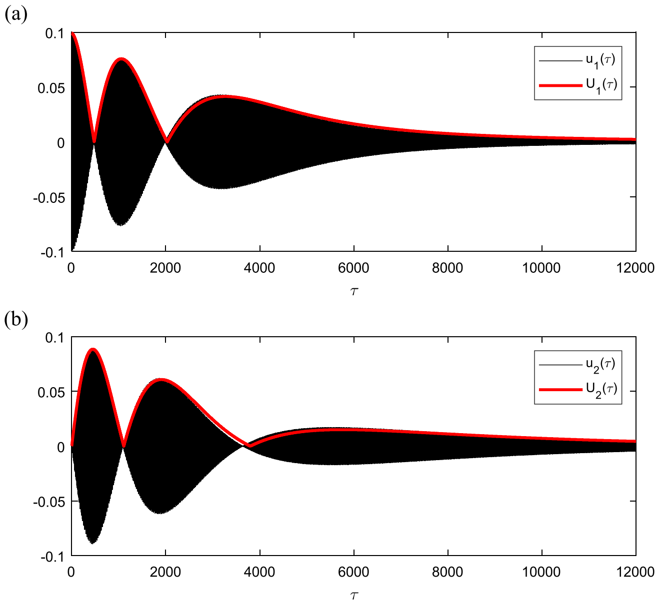

FIG. 2. (Color online) Comparison between analytically computed envelopes, Eq. (6), and the corresponding envelopes derived from direct numerical simulation of Eq. (2): (a) $u_1(\tau)$ and (b) $u_2(\tau)$.

Now, considering the analytical expressions (6) the relation between n, the impulse intensity I_0, and the damping coefficient λ can be expressed as

$$(2n-1)\frac{\pi}{2} < \frac{3N^2}{8\lambda} \le (2n+1)\frac{\pi}{2} \tag{7}$$

so that the maximum value for the ratio $3N^2/(8\lambda)$ corresponding to exactly n beats is given by

$$\frac{3N^2}{8\lambda} = (2n+1)\frac{\pi}{2}. \tag{8}$$

Relation (8) yields the "characteristic curves," with each of them dividing the parameter space, (λ, I_0), into sectors. For a fixed number of total beats, n, there corresponds a single characteristic curve—termed the nth characteristic curve. The sector (region) between the nth and $(n+1)$-th characteristic curves in the parameter plane contains values of (λ, I_0) for which a maximum number of n beats occur before *beat arrest* is realized. After *breather arrest* has occurred, the responses of the two oscillators decay to zero with no more intense energy exchanges occurring between them. Some of the characteristic curves are shown in Fig. 3. For a fixed value of total beats n, the relation between λ and I_0 can be expressed as $\lambda = a_n {I_0}^{c_1}$, where a_n is a coefficient directly related to n, while c_1 is a constant exponent which can be determined from Eq. (8) with an approximate value of $c_1 = 1.9740$.

In Sec. III we consider the semi-infinite extension of the simplified system of Fig. 1 and show that the results related

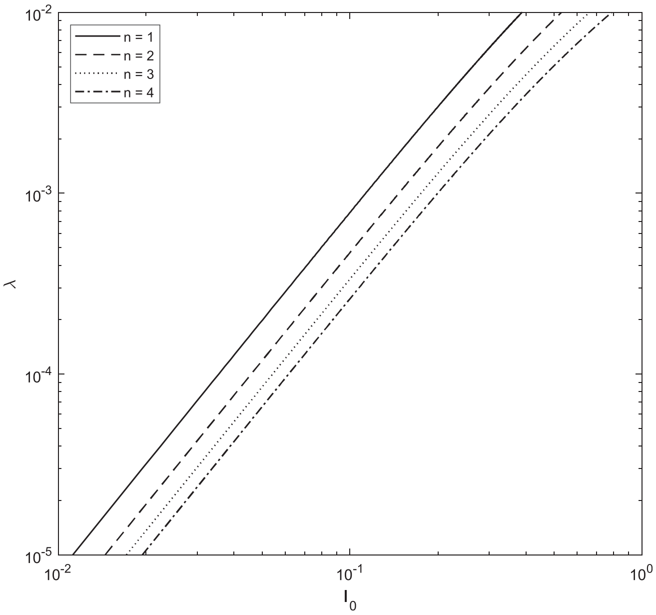

FIG. 3. Characteristic curves for specific maximum number of beatings in logarithmic scale.

to beat arrest reported herein can be related to breather arrest in the resulting semi-infinite lattice.

III. SEMI-INFINITE HOMOGENEOUS SYMMETRIC NONLINEAR LATTICE—BREATHER ARREST

The semi-infinite extension of the simplified system of Fig. 1 is the strongly nonlinear, one-dimensional lattice shown in Fig. 4. This lattice consists of identical grounded linear oscillators coupled by strongly nonlinear springs with cubic stiffness characteristics. Considering that the left boundary of the lattice is free, that an impulsive excitation is applied to the left boundary and that the system is initially at rest, the governing equations of motion are expressed as

$$\begin{aligned}&m\ddot{x}_1 + d\dot{x}_1 + kx_1 + C(x_1 - x_2)^3 = F(t) = F_0\hat{f}(t),\\&x_1(0+) = \dot{x}_1(0+) = 0,\\&m\ddot{x}_i + d\dot{x}_i + kx_i + C(x_i - x_{i-1})^3 + C(x_i - x_{i+1})^3 = 0,\\&x_i(0+) = \dot{x}_i(0+) = 0, \quad i = 2, 3, \ldots,\end{aligned} \tag{9}$$

where $\hat{f}(t)$ is a half cycle of the sine function with a period of 0.005 s and maximum amplitude equal to unity, and F_0 is the magnitude of the impulsive excitation. Figure 5 depicts the responses of the six leading particles of the lattice (counted from the left free boundary) for the applied impulsive load of amplitude 80 N and the parameters listed in Table I. Whereas all displacements are plotted in the same scale, there are depicted in vertically shifted positions for clarity of presentation. The parameters (except for the damping coefficient) listed in Table I are identical to the measured and/or identified parameters of the experimental lattice studied in Ref. 15, so that they can be physically realized. Unless otherwise noted, these will be the parameters assumed for the nonlinear lattices studied in this section. Moreover, for the numerical simulations lattices composed of twenty particles were selected (this number was sufficient for the breather arrest results discussed below).

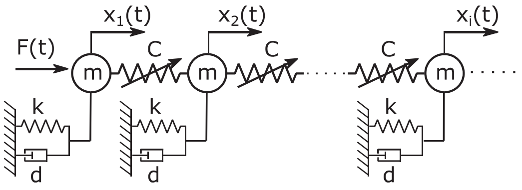

FIG. 4. Configuration of the one-dimensional semi-infinite strongly nonlinear lattice.

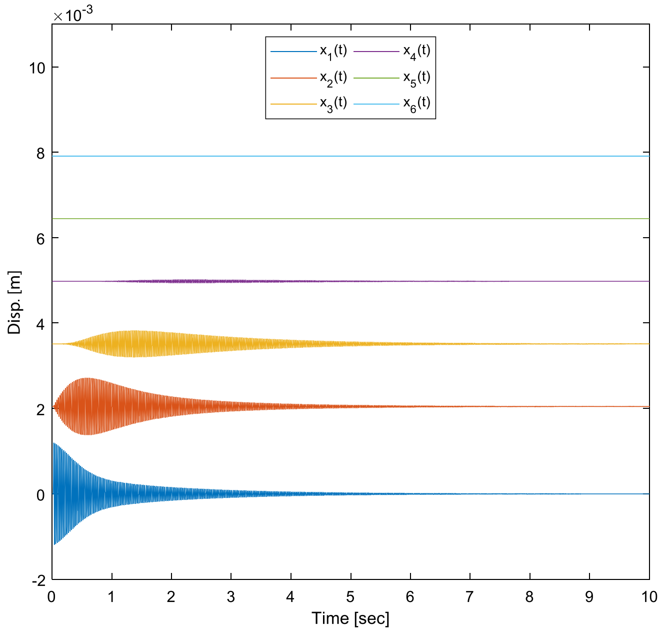

FIG. 5. (Color online) Responses of the six leading particles of the lattice for $F_0 = 80$ N.

Considering the plots of Fig. 5 we note that following the application of the impulsive excitation a traveling breather is generated, but the amplitude of the breather drastically decreases after propagating through a certain number of particles of the lattice. This disappearance of the traveling breather will be referred to as *breather arrest* from here on. Since in the infinite lattice (unlike in the simplified 2 DOF system) after breather arrest there remains an exponentially decaying oscillation at each site, a certain criterion should be considered to define the occurrence of breather arrest,

$$\frac{\max_t(|x_i(t)|)}{\max_t(|x_1(t)|)} < 10^{-4}, \quad i = 2, 3, \ldots. \tag{10}$$

It turns out that the number of particles after which the amplitude of the breather becomes negligibly small, i.e., the

TABLE I. Parameters used for the numerical simulations of the one-dimensional nonlinear lattice.

Parameter	Value
m [kg]	0.4349
k [N/m]	30166
d [Ns/m]	0.5
C [N/m^3]	5×10^8

penetration depth of the breather, highly depends on the amplitude of the impulse and the grounding damping coefficient. In the specific simulation depicted in Fig. 5, we note that the breather which is initiated by the impulse of magnitude $F_0 = 80\,\mathrm{N}$ is able to penetrate only up to four particles into the lattice (cf. Fig. 5).

Motivated by these numerical results, we performed a series of numerical simulations to study breather arrest in the semi-infinite lattice for varying applied impulses and grounding damping coefficients with all other system parameters kept fixed (cf. Table I). In Fig. 6 the penetration depth curves (i.e., the number of the leading particles reached by the breather) as functions of the impulse magnitude, F_0, and the grounding damping coefficient, d, are depicted. In each simulation, the penetration depth was numerically determined by considering the responses $x_i(t)$ of the leading particles of the lattice and establishing approximately the particle where the amplitude of the breather was nearly eliminated by satisfying Eq. (10), taking into account that the leading particle (i.e., the one that is directly excited by the applied impulsive load) attains always the maximum amplitude. The criterion (10) indicates that breather arrest occurs at the first particle whose temporal maximum response is less than 0.01% compared to the first particle.

Considering the plots of Fig. 6 one deduces similar trends to the beat arrest plots of Fig. 3 for the simplified system of Sec. II. From these results we note that, with the exception of very small forcing magnitudes and damping values, it approximately holds that $d \approx b_n {F_0}^{c_2}$, where n denotes the penetration depth of the propagating breather. Moreover, theoretically the penetration depth curves of Fig. 6 should start from $d = 0$, $F_0 = 0$ (i.e., same as in the plots of Fig. 3). This numerical error is due to inaccuracies in the numerical integrations of the equations of motion and the approximate criterion (10).

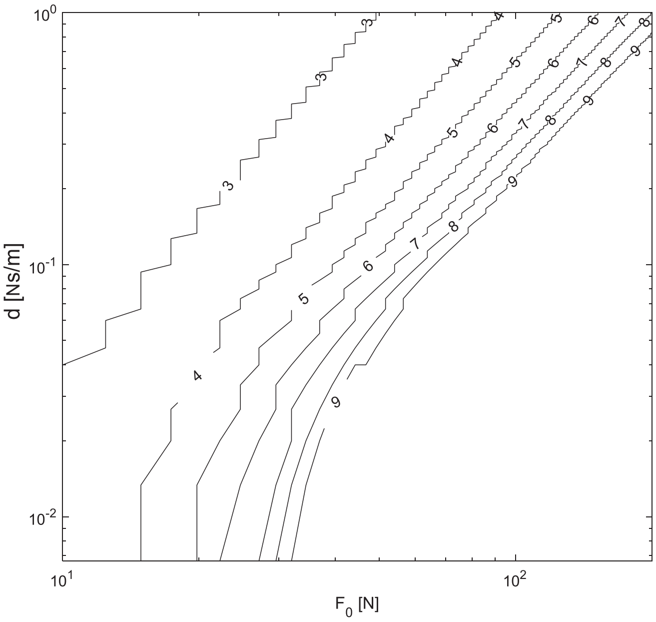

FIG. 6. Breather penetration depths in the semi-infinite homogeneous lattice in the parameter space (d, F_0) in logarithmic scales.

Neglecting the initial parts of the penetration depth level curves in Fig. 6, determining the corresponding slopes yields the approximate value of the exponent $c_2 \approx 2.0046$, which compares to the analytic value for the corresponding exponent of the beat arrest curves of the simplified system of Sec. II, $c_1 = 1.9740$. Hence, we deduce that *the study of beat arrest in the simplified 2 DOF system can predict fairly accurately breather arrest in the semi-infinite one-dimensional chain*, with an error of approximately 1.5%. On the other hand, the dimensional form of the coefficients a_n for the simplified system do not directly correspond to the coefficients b_n for the homogeneous semi-infinite system. The main reason that causes this discrepancy is that in the simplified system, the only dissipative source that reduces the energy carried by the beats is the on-site damping of the two particles, whereas in the lattice, in addition to on-site damping of the particles there is "radiation damping" as the breather passes from each particle since it leaves an oscillatory tail behind it with frequency approximately equal to the linear frequency of each oscillator (i.e., there is an additional "ringing" effect). The equivalent term for this tail in the simplified system is the exponentially decaying non-beating term which only appears once for each particle while the tail appears for each of the particles of the lattice mass during breather propagation (cf. Fig. 5). In other words, in the lattice, the energy of the breather is reduced by the on-site damping of each particle as well as the tail that remains after the breather passes by each of the particles.

In conclusion, the results of this section established a surprising approximate correspondence between beat arrest in the simplified system and breather arrest in the homogeneous nonlinear lattice which represents a semi-infinite extension of the simplified system. Moreover, the dissipative mechanisms that influence breather arrest were discussed. In Sec. IV we consider a finite hierarchical, strongly nonlinear system with a hierarchical structure that incorporates asymmetry. We show that the study of breather arrest in this lattice is directly linked to interesting acoustic non-reciprocity phenomena that occur when the point of the applied impulse excitation varies.

IV. FINITE HIERARCHICAL, ASYMMETRIC AND NONLINEAR LATTICE—BREATHER ARREST AND ACOUSTIC NON-RECIPROCITY

The final system considered in this work is the one-dimensional (1D) nonlinear lattice depicted in Fig. 7, incorporating both scale hierarchy and asymmetry. The lattice is composed of a finite number (N) of repetitive cells, with each cell consisting of a large particle [designated as the internal "large-scale" (LS)] nonlinearly coupled to a smaller particle [the internal "small-scale" (SS)]. The nonlinear stiffness coupling the two internal scales in each cell has a strongly nonlinear stiffness characteristic, which for the time being is assumed to be *essentially nonlinear* and *non-linearizable* (i.e., its nonlinear stiffness characteristic is purely cubic without any linear component); in Sec. IIIC we consider the (surprisingly important) effects of a small linear component in the coupling stiffness characteristic. Moreover, the SS of each cell is

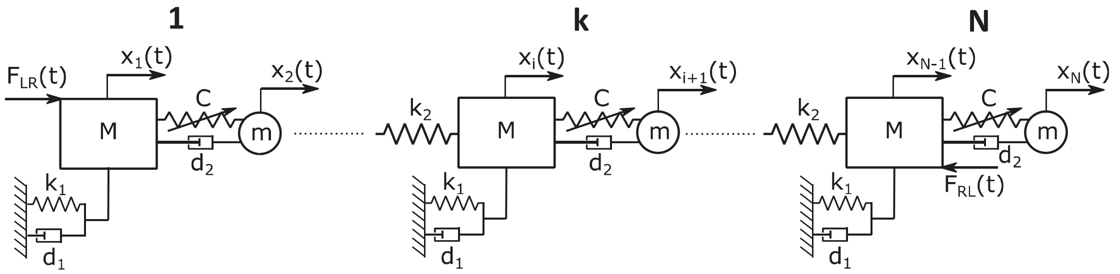

FIG. 7. Configuration of the finite nonlinear hierarchical and asymmetric lattice with cell 1 being the left-most and cell N the right-most one.

coupled to the LS of the cell on its right by a linear stiffness, except for the last cell (cf. Fig. 7), and the LS of each cell is grounded by a linear spring-viscous damper pair in parallel. Finally, only impulsive external forcing excitation is considered as discussed below. Recently this lattice has been the subject of experimental[15] and computational[30] study.

Assuming unidirectional motion, the equations of motion governing the acoustics of this lattice are given by

$$\begin{aligned}
&M\ddot{x}_1 + d_1\dot{x}_1 + d_2(\dot{x}_1 - \dot{x}_2) + k_1x_1 + C(x_1 - x_2)^3 = F_{LR}(t),\\
&m\ddot{x}_2 + d_2(\dot{x}_2 - \dot{x}_1) + C(x_2 - x_1)^3 + k_2(x_2 - x_3) = 0,\\
&\vdots\\
&M\ddot{x}_i + d_1\dot{x}_i + d_2(\dot{x}_i - \dot{x}_{i+1}) + k_1x_i + C(x_i - x_{i+1})^3 + k_2(x_i - x_{i-1}) = 0,\\
&m\ddot{x}_{i+1} + d_2(\dot{x}_{i+1} - \dot{x}_i) + C(x_{i+1} - x_i)^3 + k_2(x_{i+1} - x_{i+2}) = 0,\ 3 \le i \le N-2,\\
&\vdots\\
&M\ddot{x}_{N-1} + d_1\dot{x}_{N-1} + d_2(\dot{x}_{N-1} - \dot{x}_N) + k_1x_{N-1} + C(x_{N-1} - x_N)^3 + k_2(x_{N-1} - x_{N-2}) = F_{RL}(t),\\
&m\ddot{x}_N + d_2(\dot{x}_N - \dot{x}_{N-1}) + C(x_N - x_{N-1})^3 = 0,\\
&x_j(0+) = \dot{x}_j(0+) = 0, \quad j = 1, 2, \ldots, N,
\end{aligned} \tag{11}$$

where the parameters are the same as the ones used in Ref. 15 and are defined in the schematic of Fig. 7. Unless otherwise noted, the lattice is assumed to be composed of $N = 20$ cells, and the numerical values for the system parameters are listed in Table II; these parameters were identified for the experimental realization of the three-cell hierarchical lattice studied in Ref. 15 (but for a small linear stiffness component in the nonlinear stiffnesses connecting the SSs and the LSs whose effect is discussed in Sec. IV C). Zero initial conditions are assumed, and the lattice is forced by either "left" impulsive excitation with $F_{LR}(t) = F_0\hat{f}(t)$ and $F_{RL}(t) = 0$, or "right" impulsive excitation with $F_{RL}(t) = -F_0\hat{f}(t)$ and $F_{LR}(t) = 0$; F_0 (in N) is the impulsive amplitude, and $\hat{f}(t)$ is the broadband function defined in Sec. III.

TABLE II. System parameters of the nonlinear asymmetric hierarchical lattice (Ref. 15).

Parameter	Value
M [kg]	0.4349
m [kg]	0.0204
k_1 [N/m]	30166
d_1 [Ns/m]	0.5
C [N/m^3]	5×10^8
k_2 [N/m]	3753.75
d_2 [Ns/m]	0.0014

Due to the asymmetry in the hierarchical nonlinear lattice, we anticipate that the signal transmission properties will be energy dependent (i.e., will depend on the intensity of the impulsive excitation), but also on the location of the impulsive excitation. Hence, we need to consider separately the cases of right-to-left and left-to-right wave propagation, corresponding to right or left impulsive excitation, respectively.

A. Right-to-left wave transmission

For right impulsive excitation the only force acting on the hierarchical lattice is applied to the LS of the last cell, i.e., the rightmost LS which on its right is nonlinearly connected to the ultimate (rightmost) free SS, and on its left is linearly connected to the SS of the penultimate cell. In Fig. 8 we illustrate the spatio-temporal evolution of the instantaneous total energy, normalized with respect to remaining total energy at a given time instant. The lattice considered in the simulations has the parameters listed in Table II, except for the grounding damping which is assigned the value $d_1 = 0.15\,\mathrm{Ns/m}$. Moreover, we consider the responses for both large and small impulsive

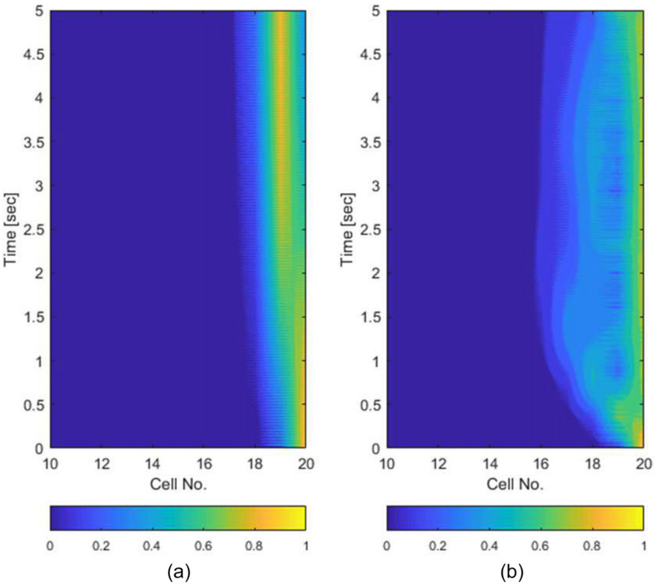

(a) (b)

FIG. 8. (Color online) Right-to-left wave transmission in the finite hierarchical lattice: spatio-temporal evolution of the normalized instantaneous total energy of the lattice for right impulsive excitation for $\boldsymbol{d}_1 = 0.15\,\mathrm{N\ s/m}$ and (a) $\boldsymbol{F}_0 = 35\,\mathrm{N}$—point (p$_1$) in Fig. 9, (b) $\boldsymbol{F}_0 = 150\,\mathrm{N}$—point (p$_2$) in Fig. 9; only cells 10–20 are depicted and the square root of the normalized data is plotted for better visualization.

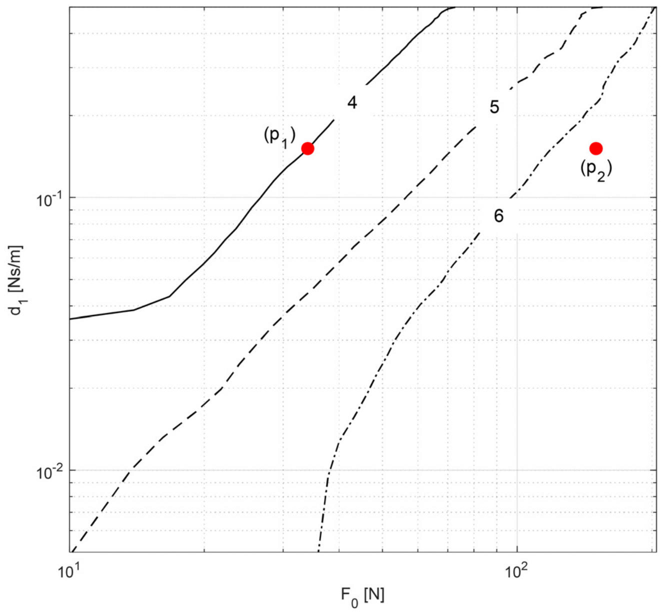

FIG. 9. (Color online) Right-to-left wave transmission in the finite hierarchical lattice: breather penetration depth curves in the parameter space (d_1, F_0) in logarithmic scales; points (p$_1$) and (p$_2$) refer to the cases of breather arrest depicted in Figs. 8(a) and 8(b), respectively.

amplitudes, namely, $F_0 = 150$ and 35 N. For clarity in the plots of Fig. 8 we depict only cells 10–20. Immediately following the application of the impulsive excitation there occurs *breather initiation* at the rightmost cell 20, with the breather propagating in the lattice with decreasing speed as its energy is dissipated due to damping. For the case of small impulse excitation the breather is arrested at cell 16, whereas for the larger impulsive excitation the breather is arrested at cell 14 (refer to Fig. 10 below).

To study the effects on the penetration depth of the breather of the grounding damping d_1 and forcing amplitude force F_0, in Fig. 9 we depict the breather penetration depth curves for cells 4, 5, and 6 (as defined in Sec. III) in the parameter space (d_1, F_0). Similar to Figs. 3 and 6, in the logarithmic plots of Fig. 9 we observe a linear asymptotic behavior for each penetration depth level curve. Hence, neglecting the initial segment in each curve (which is due to the finite time window of the corresponding numerical integrations), a relation of the form $d_1 = \alpha_n {F_0}^{c_3}$, where the exponent is approximately determined as $c_3 \approx 1.85$ by computing the corresponding slopes in the logarithmic plot. Notice that there is a slight difference in the slopes of the lines shown in Fig. 9, so the previous value of c_3 represents the averaged value obtained.

A typical example of right-to-left breather generation, propagation and ultimate arrest is given in Fig. 10 for the case corresponding to point (p$_1$) in Fig. 9, and the spatiotemporal normalized energy plots of Figs. 8(a) and 8(b) which correspond to points (p$_1$) and (p$_2$), respectively. The time series in Fig. 10 depict the responses of the LSs of the five right cells of the hierarchical lattice, and although the time series of each figure are plotted in the same scale, all but the last are shifted horizontally for clarity. The generated breather following the application of the impulsive excitation is clearly discernable, having the form of an oscillating wavepacket which is modulated by a slow decaying envelope. Since point (p$_1$) is located on the breather penetration curve for four cells in the parameter space of Fig. 9, one expects that the propagating breather will be able to penetrate only up to four cells into the lattice for the case of low impulsive excitation and then be arrested at the location of that cell. Indeed, the transient responses of the LSs of the cells depicted in Fig. 10 confirm the relatively large amplitude of the breather for the right-most LSs, and its nearly negligible amplitude for the LSs of the remaining cells.

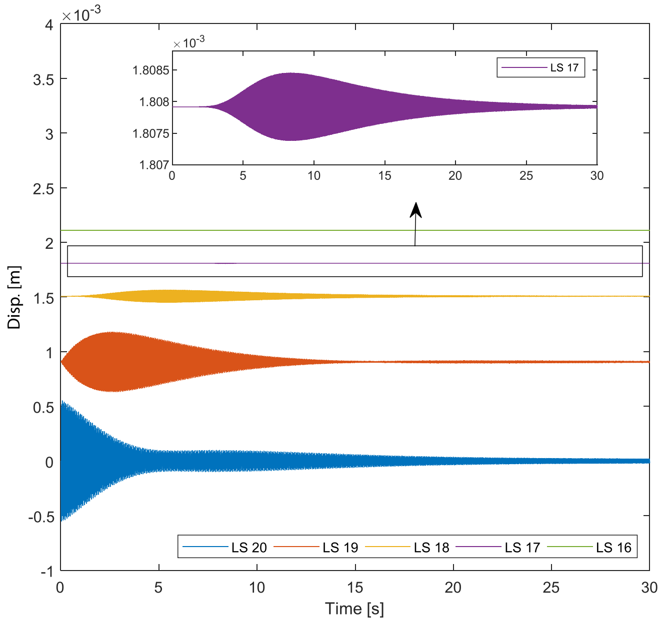

FIG. 10. (Color online) Right-to-left wave transmission in the essentially nonlinear lattice showing breather arrest for point (p$_1$) in Fig. 9; depicted are the responses of the LSs of the rightmost cells—note the magnification boxes for the LS of cell 17.

B. Left-to-right wave localization

We now consider left impulsive excitation of the hierarchical lattice in order to highlight its strongly non-reciprocal acoustics. In Fig. 11 the spatio-temporal evolution of the instantaneous energy of the lattice is depicted for identical system parameters to the ones designated by point (p_2) in Fig. 9 (i.e., for $F_0 = 150\,\mathrm{N}$, $d_1 = 0.15$ Ns/m, and the other system parameters listed in Table II). Compared to the spatiotemporal plots of Figs. 8(a) and 8(b) we deduce a qualitatively different lattice response in this case. Indeed, in contrast to the breather formation and arrest for the case of right impulsive excitation, in this case we note *standing wave localization* and *spatial energy confinement* for left impulsive excitation.

Comparing the spatiotemporal energy plots of Figs. 8 and 11 it is clear that, while for the case of right-to-left wave transmission the initiated breather propagates into the lattice until its eventual arrest, in the left-to-right case there is complete absence of breather initiation and propagation; rather, a localized standing wave forms, spatially extending up to the leading four cells of the lattice and energy is spatially confined and is not getting transmitted into the lattice. The non-reciprocal features of the nonlinear acoustics of the hierarchical lattice are highlighted by comparing the right-to-left breather penetration depth curves of Fig. 9 to the corresponding left-to-right spatial extension curves for the localized standing wave depicted in Fig. 12. Point (q) in Fig. 12 coincides with point (p_2) in Fig. 9, but a different notation is used to distinguish between the right-to-left and left-to-right cases.

A typical example of left-to-right standing wave localization in the lattice is given in Fig. 13 for the case corresponding to point (q) in Fig. 12 and the spatio-temporal energy plot depicted in Fig. 11. The time series in that figure depict the responses of the LSs of the five leading cells of the lattice for a left impulsive excitation (as in the plots of Fig. 10 the time series are presented in the same scale, and all but the first are shifted horizontally for clarity). The formation of the standing wave following the application of the impulsive excitation is clearly discernable, with the three leading LSs oscillating approximately in-unison with absence of any wave transmission into the lattice. In contrast to right impulsive excitation there is no breather initiation in this case, and instead a spatially confined standing waveform is formed which decays after the leading three cells of the

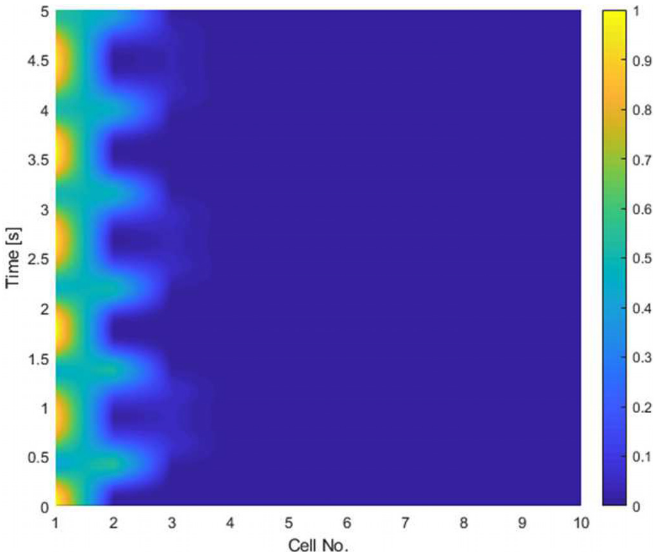

FIG. 11. (Color online) Left-to-right localized standing wave formation in the finite hierarchical lattice: spatio-temporal evolution of the normalized instantaneous total energy of the lattice for right impulsive excitation for $\boldsymbol{d}_1 = 0.15$ N s/m and $\boldsymbol{F}_0 = 150$ N—point (q) in Fig. 10; only cells 1–10 are depicted and the square root of the normalized data is plotted for better visualization.

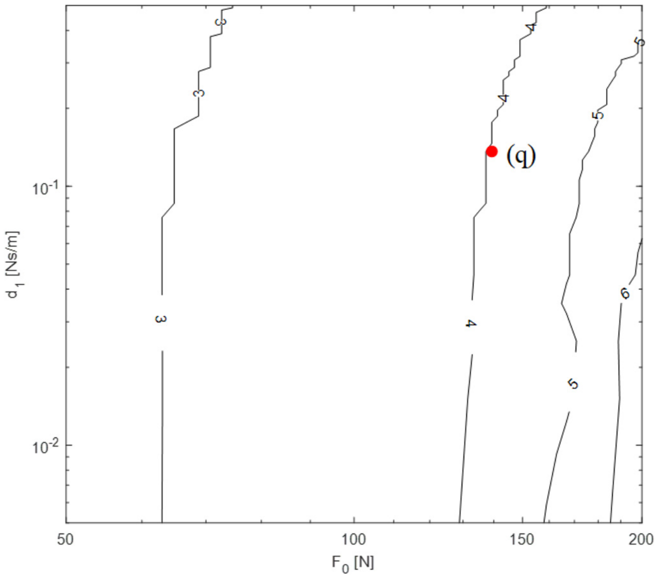

FIG. 12. (Color online) Left-to-right standing wave localization in the finite hierarchical lattice: spatial extension curves of the standing wave in the parameter space (d_1, F_0) in logarithmic scales; point (q) refers to the spatio-temporal energy plot of Fig. 11 and the time series of Fig. 13 [note that point (q) coincides with point (p_2) in Fig. 9].

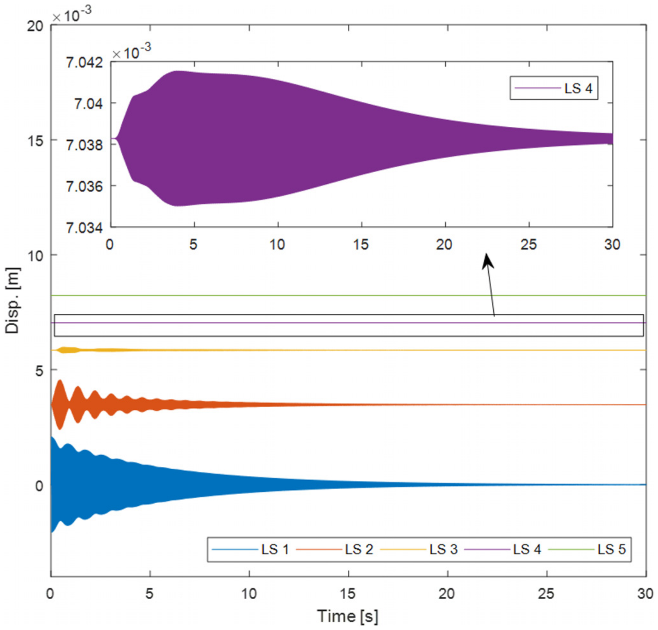

FIG. 13. (Color online) Left-to-right wave localization in the finite hierarchical lattice: localized standing wave confined in the leading three cells corresponding to point (q) of Fig. 12; the depicted time series represent the responses of the LSs of the five leftmost cells of the lattice (note the magnification box for LS of cell 4).

lattice. It is interesting to note the occurrence of a finite number of beats (i.e., of recurring intense energy exchanges) in the responses of the LSs of the leading cells 1 and 2, which resemble the beat phenomena and arrest noted in the responses of the simplified system of Sec. II. This strongly suggests that the left-to-right wave localization in the hierarchical lattice may be studied by a simplified reduced-order model analogous to the one considered previously.

We comment briefly on the non-reciprocal acoustical features of the lattice as evidenced by the right-to-left wave transmission compared to the left-to-right wave localization. This appears to be caused by the asymmetry of the lattice at its left and right boundaries, i.e., the way that the LSs and SSs in the leading and last cells are connected. To this end, we note that for *left impulsive excitation* the directly excited LS of the first cell (designated as LS1) is nonlinearly coupled to the SS of the first cell (i.e., SS1), which itself is linearly coupled on its right to LS2; whereas due to the asymmetry of the lattice for *right impulsive excitation* the directly excited LS20 is nonlinearly coupled on its right to SS20 (which is free to oscillate) and on its left is linearly coupled to SS19. As such, due to its linear coupling to LS20, SS19 is capable of resonating with LS20 and, consequently, of gaining more energy for relatively small input forces, compared to the case where the force is applied to LS1. The *linear resonance* effect between SS19 and LS20 appears to be the main mechanism for the generation and initiation of the breather for right impulsive excitation, whereas its absence for right impulsive excitation (where SS1 is nonlinearly coupled to LS1 and linearly coupled to LS2) leads to wave localization in that case.

C. The effect of a linear component in the nonlinear coupling stiffness

In this section we reconsider the finite hierarchical asymmetric lattice composed of N cells, but now we add a linear component with characteristic k_3 in the nonlinear coupling stiffnesses between the SSs and LSs; hence, we consider the lattice with *linearizable nonlinearities*, which from here on we will be referring as the "*modified lattice*." Adopting the same notation as for the essentially nonlinear lattice of Fig. 7, and assuming a total of $N = 20$ cells, the parameters of the modified lattice are identical to those listed in Table II, with the only addition being the linear stiffness coefficient $k_3 = 1598.2\,\mathrm{N/m}$. As for the other system parameters listed in Table II, this coefficient was identified for the experimental lattice studied in Ref. 15. Accordingly, the governing equations of motion of the modified lattice are expressed as

$$
\begin{aligned}
&M\ddot{x}_1 + d_1\dot{x}_1 + d_2(\dot{x}_1 - \dot{x}_2) + k_1x_1 + k_3(x_1 - x_2) + C(x_1 - x_2)^3 = F_{LR}(t),\\
&m\ddot{x}_2 + d_2(\dot{x}_2 - \dot{x}_1) + k_3(x_2 - x_1) + C(x_2 - x_1)^3 + k_2(x_2 - x_3) = 0,\\
&\vdots\\
&M\ddot{x}_i + d_1\dot{x}_i + d_2(\dot{x}_i - \dot{x}_{i+1}) + k_1x_i + k_3(x_i - x_{i+1}) + C(x_i - x_{i+1})^3 + k_2(x_i - x_{i-1}) = 0,\\
&m\ddot{x}_{i+1} + d_2(\dot{x}_{i+1} - \dot{x}_i) + k_3(x_{i+1} - x_i) + C(x_{i+1} - x_i)^3 + k_2(x_{i+1} - x_{i+2}) = 0, \quad 3 \le i \le N-2,\\
&\vdots\\
&M\ddot{x}_{N-1} + d_1\dot{x}_{N-1} + d_2(\dot{x}_{N-1} - \dot{x}_N) + k_1x_{N-1} + k_3(x_{N-1} - x_N) + C(x_{N-1} - x_N)^3 + k_2(x_{N-1} - x_{N-2}) = F_{RL}(t),\\
&m\ddot{x}_N + d_2(\dot{x}_N - \dot{x}_{N-1}) + k_3(x_N - x_{N+1}) + C(x_N - x_{N-1})^3 = 0,\\
&x_j(0+) = \dot{x}_j(0+) = 0, \quad j = 1, 2, \ldots, N,
\end{aligned}
\tag{12}
$$

where, as in Secs. IV A and IV B, we consider left and right impulsive excitations in order to study the nonlinear acoustic non-reciprocity in this case.

Following the same logic, we examine the behavior of the system for left-to-right and right-to-left wave transmission or localization by performing direct numerical integrations of the equations of motion (12). Figures 14(a) and 14(b) depict the spatio-temporal evolution of normalized total energy of the modified lattice for an intermediate impulsive amplitude of $F_0 = 100$. That is, to get a more detailed depiction of wave generation and transmission in the lattice, at each time instant the instantaneous energy of the lattice is normalized with respect to the total energy remaining in the lattice at that time instant. Such normalization accounts for the dissipation of the total energy by the viscous dampers of the cells.

Although the results of Figs. 14 confirm the (anticipated) strong acoustic non-reciprocity of the modified lattice at this level of applied energy, the unexpected finding is that *the wave localization and transmission features in this case are reversed* compared to the original (essentially nonlinear) lattice. Indeed, the modification of the lattice by small linear coupling terms, yields *right-to-left wave localization* [cf. Fig. 14(a)] and *left-to-right wave transmission* [cf. Fig. 14(b)], which is the reverse of what was found for the essentially nonlinear lattice in Secs. IV A and IV B. A closer examination of the plot of Fig. 14(b) reveals slight right-to-left wave transmission but this is immediately dissipated

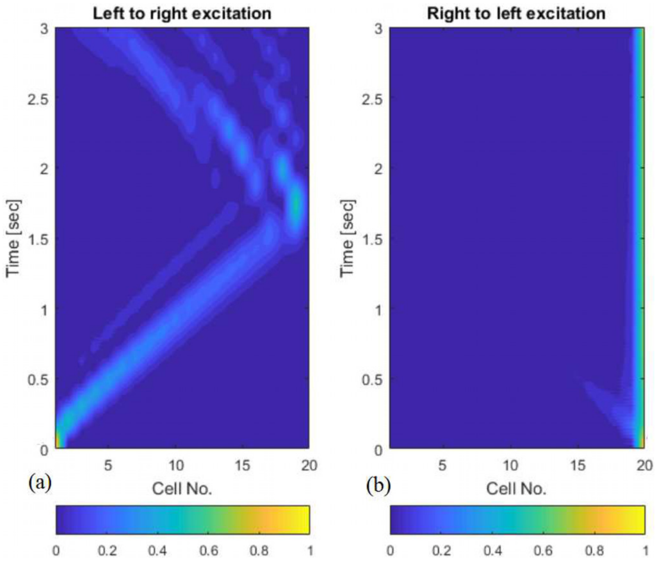

FIG. 14. (Color online) Non-reciprocal acoustics of the modified lattice: spatio-temporal evolution of the normalized instantaneous total energy of the lattice for (a) left impulsive excitation, (b) right impulsive excitation for the intermediate impulsive amplitude $\boldsymbol{F}_0 = 100$ N.

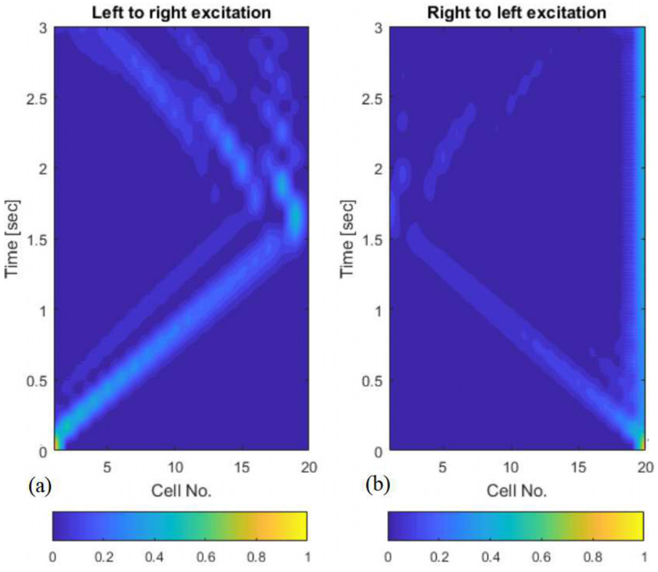

FIG. 15. (Color online) Non-reciprocal acoustics of the modified lattice: spatio-temporal evolution of the normalized instantaneous total energy of the lattice for (a) left impulsive excitation, (b) right impulsive excitation for the high impulsive amplitude $\boldsymbol{F}_0 = 350$ N.

before it can further penetrate into the modified lattice. As previously, this should be caused by the asymmetry of the modified lattice, since for right excitation on LS20, SS20 is free to oscillate, whereas for left excitation on LS1, SS1 is restricted by coupling elements both on its right and on its left. This indicates that for the case of right excitation SS20 can potentially act as a *nonlinear energy sink* (NES),[31,32] rapidly absorbing a significant portion of the impulsive energy, hindering the transmission of energy (waves) into the lattice, and causing wave localization in the directly excited LS20. That would amount to a very interesting nonlinear boundary effect, which might be the mechanism for acoustic non-reciprocity in this case; however, clearly there is a different mechanism for reciprocity in the modified lattice.

Prior to performing a more detailed investigation of the mechanism for acoustic non-reciprocity in the modified lattice, we wish to emphasize the effect of energy on the non-reciprocal acoustics. Accordingly, in Figs. 15(a) and 15(b) we present the spatio-temporal normalized energy evolutions for the modified lattice for the higher impulsive amplitude $F_0 = 350$ N. Whereas left-to-right wave transmission is preserved at this higher energy level, there is increased wave transmission into the lattice for right excitation, despite the fact that a significant portion of the impulsive energy remains localized at the right boundary. This underscores the importance of the energy level, since at it appears that at increased energy there is more intense right-to-left wave transmission.

These results indicate that, despite the preservation of acoustic non-reciprocity in the modified lattice, the addition of small linear components in parallel to the nonlinear coupling stiffnesses qualitatively modifies the non-reciprocal acoustics. This major change in the acoustics of the modified lattice resulting from such a slight structural modification strongly suggests that a different nonlinear mechanism governs the acoustics in this case. Having this in mind, we investigate in more detail the non-reciprocal acoustic features of the modified (linearizable) lattice, and their dependence on the amplitude of the impulsive excitation (i.e., the energy level).

To gain an understanding of acoustic non-reciprocity in the modified lattice we need to construct a frequency-energy plot—FEP depicting its nonlinear periodic orbits in the frequency—energy plane, namely, its *nonlinear normal modes* (NNMs),[33] in the absence of dissipative or external forces. It turns out that for the 40-DOF modified lattice there exist 40 NNMs (which are ordered with respect to increasing linearized natural frequency in their low energy limits) and six of them are depicted in Fig. 16 together with the corresponding mode shapes in Fig. 17. These results were derived by setting $d_1 = 0$, $d_2 = 0$, $F_0 = 0$ in the system (12) and computing the periodic responses of the resulting Hamiltonian system by numerical continuation.[34] The six NNMs, namely, the NNMs 1, 2, 20, 21, 22, and 40, are depicted in the FEP of Fig. 16 represent special periodic responses of the lattice.

The NNM 2 (20) is the lowest- (highest-) frequency mode of the lower-frequency family of modes whose mode shape is spatially extended, and each SS oscillates in-phase with respect to the LSs of the neighboring cells; what distinguishes these particular modes in this family is that for NNM 2 all LSs oscillate in-phase with respect to each other, whereas for NNM 20 all LSs oscillate out-of-phase. As discussed in a previous work[35] NNMs 2 and 20 define the lower and upper boundaries, respectively, of the (lower-frequency) *nonlinear acoustical passband* of the modified lattice. Similarly, the pair of higher-frequency NNMs 22 and 40 defines the (higher-frequency) *nonlinear optical passband* of the modified lattice. We note at this point that such passbands define the ranges of frequencies and energies for which waves can propagate in the *infinite* modified lattice; in the finite lattice considered herein (composed of only 20 cells), one can only refer to such passbands in an approximate sense, although it is worth pointing out that spatially

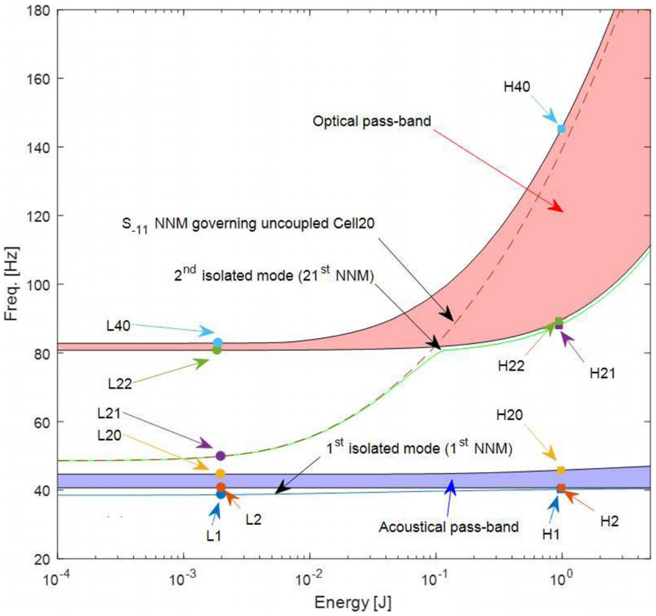

FIG. 16. (Color online) Frequency-energy plot (FEP) of the modified nonlinear lattice with the two localized NNMs 1 and 21, the NNMs 2 and 20 approximately bounding the acoustical passband, and the NNMs 22 and 40 approximately bounding the optical passband; L1-L40 and H1-H40 refer to the mode shapes of Fig. 17 (------: frequency-energy curve for grounded SS20).

extended NNMs of the finite lattice are always situated in these passbands (this was the basis for the approximate computation of the passbands in terms of the highest- and lowest-frequency NNMs of each families of modes situated in each of them); in particular the lower 19 spatially extended NNMs 2–20 are located inside the acoustical passbands and the upper 19 spatially extended NNMs 21–40 inside the optical passband. Separating the passbands are three stopbands, which depending on their positions in the FEP will be referred to as *lower, intermediate, and upper stopbands*. As discussed below, the approximate passbands can help us to understand the nonlinear mechanism governing acoustic non-reciprocity in the finite modified lattice. Returning to the two NNMs that approximately define the higher-frequency nonlinear optical passband, the NNM 22 (40) is the lowest- (highest-) frequency mode of the higher-frequency family of NNMs whose mode shape is spatially extended, and each SS oscillates in an out-of-phase fashion with respect to the LSs of its neighboring cells; again, what distinguishes these modes in this family of modes is that for NNM 22 all LSs oscillate out-of-phase with respect to each other, whereas for NNM 40 all LSs oscillate in-phase.

Regarding the "isolated" NNMs 1 and 21, these are unique modes in the sense that they do not belong to a

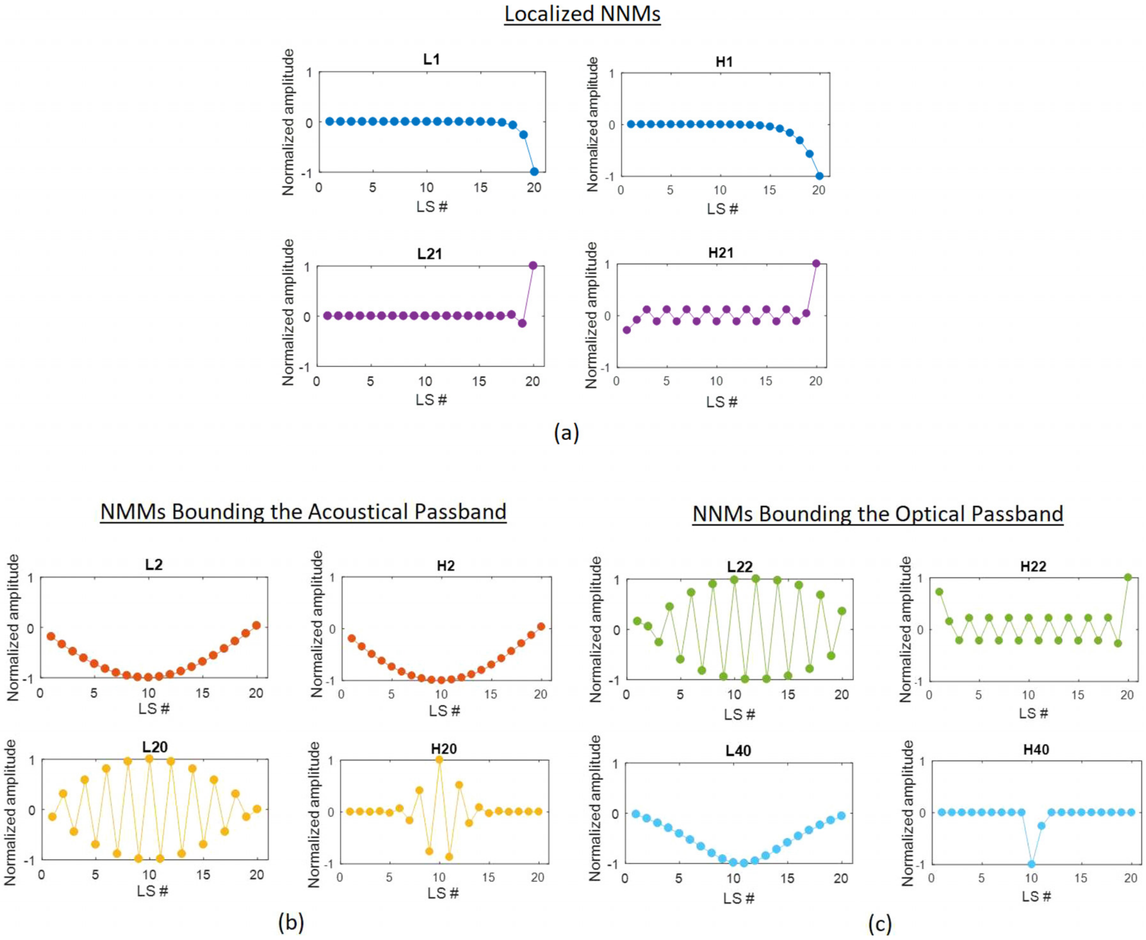

FIG. 17. (Color online) Lower-energy (L1-L40) and higher-energy (H1-H40) mode shapes of the NNMs at the selected points depicted in Fig. 16: (a) NNMs 1 and 21 localized at SS20, (b) NNMs 2 and 20 approximately bounding the acoustical passband, and (c) NNMs 22 and 40 approximately bounding the optical passband.

specific family of NNMs, and whose main feature is that they are spatially localized at SS20, i.e., at the right-most SS, which is "free" to oscillate due to the asymmetric way of the linear coupling between cells (no other SS of the lattice has this property); as mentioned previously, for this reason SS20 may act as an NES[30,32] for the modified lattice. NNM 1 (20) is the lowest- (highest-) frequency of the two.

An important feature of the NNMs depicted in the FEP of Fig. 16 is that their mode shapes (and frequencies) depend on energy. These mode shapes are depicted in Fig. 17 where we deduce that certain NNMs change drastically as energy increases. Specifically, considering the localized NNM 21 changes its waveform from spatially localized to spatially extend with increasing energy, whereas the reverse is encountered for NNMs 20 and 40 whose waveforms become spatially localized with increasing energy. We conclude by commenting on the special (and peculiar) behavior of the NNM 21, which at low-energy is spatially localized at SS20, whereas after "encountering" the upper optical band changes to being spatially extended. As discussed below, this energy-dependency has implications on the acoustic nonreciprocity in the modified lattice.

Revisiting now the impulsive response of the modified lattice (cf. Figs. 14 and 15), in Fig. 18 we depict the relative response between LS20 and SS20 subject to right impulsive excitation $F_{RL}(t)$ with $F_0 = 100\,\text{N},\ 180\,\text{N}$ and $350\,\text{N}$, and their corresponding wavelet spectra contours. The wavelet contours are superimposed to the FEP of the underlying Hamiltonian lattice of Fig. 16 with the nonlinear acoustical and optical passbands depicted (their complements form the three stopbands). To construct these wavelet depictions, time in the wavelet spectrum of the transient relative response was replaced by the total instantaneous energy of the modified lattice following the application of the impulsive excitation. It follows that decreasing (increasing) instantaneous energy corresponds to increasing (decreasing) time, with the initial state of the response occurring at the point of maximum energy on the right horizontal axis. These results clarify breather initiation in the modified lattice for right impulsive excitation.

Considering first the case of low impulsive excitation of Fig. 18(a), we note that the spectrum of the relative response is mainly confined in the lower and intermediate stopbands, with the impulse exciting mainly the second localized NNM 21 (and its harmonics) which for low energies is spatially confined in the directly excited 20th cell [cf. Figs. 16 and 17(a)]. As a result, for sufficiently small impulsive excitation no wave propagation can be initiated in the modified lattice,

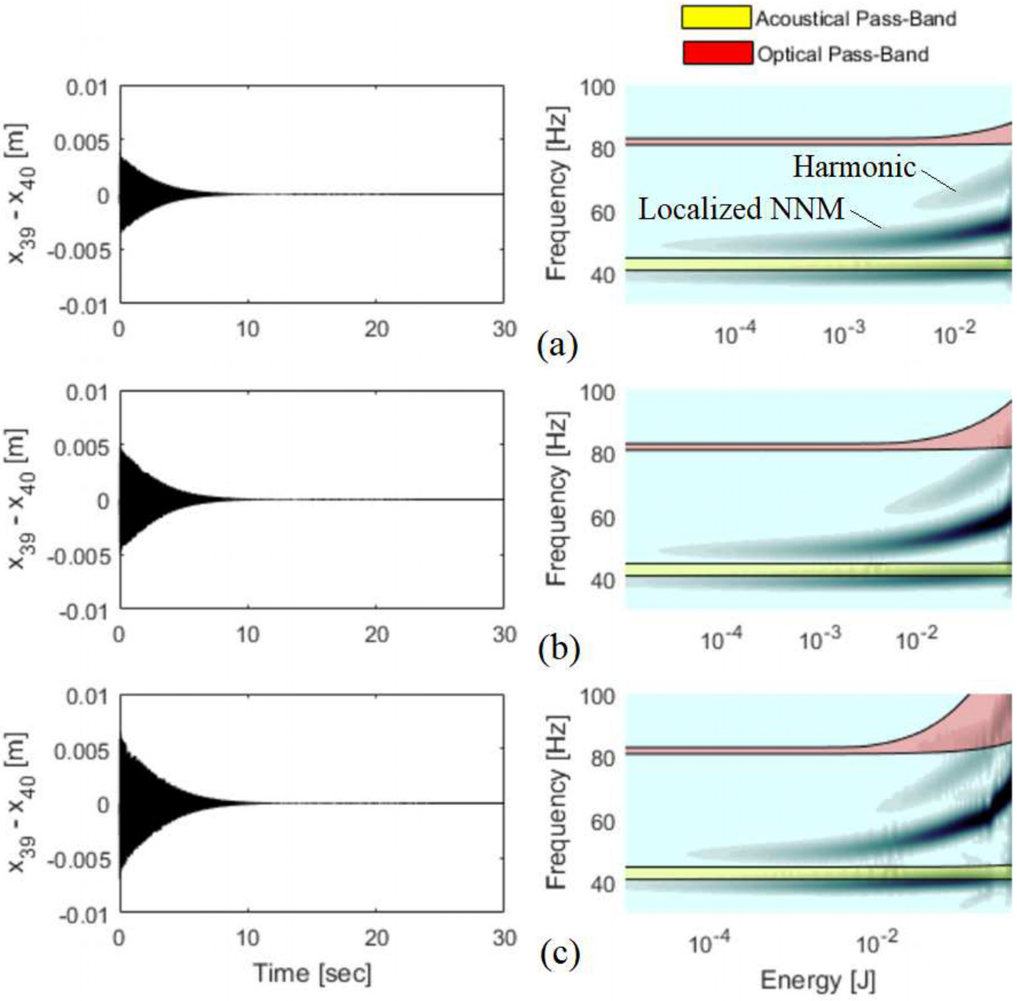

FIG. 18. (Color online) Relative responses between LS20 and SS20 of the modified lattice and the corresponding contours of the wavelet spectra for right impulsive amplitude (a) $F_0 = 100$ N, (b) $F_0 = 180$ N, and (c) $F_0 = 350$ N; the wavelet spectra are superimposed on the FEP of the underlying Hamiltonian system showing the nonlinear acoustical and optical passbands.

since for this to occur some harmonic components of the response need to be located inside the upper passband so intense energy transmission in the lattice can commence (in the lower passband there occurs much less intense wave transmission in the lattice). This result is consistent with the localized response and the weak wave transmission observed in the spatiotemporal plot of Fig. 14(b). The response changes qualitatively for increasing impulsive amplitude since for $F_0 = 180\,\mathrm{N}$ a harmonic of the localized NNM encounters the lower boundary of the upper passband at the initial stage of the response [cf. Fig. 18(b)]. This is a *point of bifurcation* and signifies the critical amplitude of the impulse beyond which intense wave transmission in the modified lattice occurs. It is worth recalling, that with increasing energy the second localized NNM 21 changes its mode shape and from localized become spatially extended [cf. the FEP of Fig. 16 and the corresponding mode shapes of Fig. 17(a)]. Hence, with increasing amplitude of the right impulse the wave localization in cell 20 is gradually eliminated. This is corroborated by the numerical results. Indeed, for the stronger impulsive amplitude $F_0 = 350\,\mathrm{N}$ [cf. Fig. 18(c)], we note that in the initial, highly energetic regime of the response the harmonic of the localized NNM is initially situated inside the upper passband, but as energy decreases due to damping this harmonic makes a transition to the intermediate stopband where it remains until energy is completely dissipated. This indicates that there traveling waves are formed in the initial regime of the motion, but this wave transmission is eliminated shortly thereafter with the motion becoming localized close to the right boundary of the lattice. This is consistent with the spatiotemporal energy plot of Fig. 15(b).

A radically different picture for the acoustics is noted for left impulsive excitation. In Fig. 19 we depict the relative response between LS1 and SS1 subject to $F_{LR}(t)$ with $F_0 = 350\,\mathrm{N}$, together with its corresponding wavelet spectrum contour. In this case there is absence of any type of localized NNM in cell 1 since SS1 is not "free" to oscillate (as is SS20 due to the asymmetric coupling of the lattice) since it is linearly coupled on its right to LS2. As a result, the harmonic components of the relative response are now located mainly inside the upper and lower passbands throughout the duration of the motion, and there are no consistent harmonic components in the stopbands, except for a brief period in the initial stage of the response (this is in contrast to the wavelet spectra of Figs. 18(a) and 18(c)]. Hence, for left impulsive excitation there is intense propagation of traveling wavepackets in the lattice in the corresponding passbands (mainly in the upper one), a result which agrees with the spatio-temporal energy plots of Figs. 14(a) and 14(b).

The previous results clarify that the principal nonlinear mechanism for acoustic non-reciprocity in the modified lattice is the localized NNM 21 at the small scale on the right boundary, which, in turn is caused exclusively by the asymmetric way of the linear coupling between cells. Hence, the acoustic non-reciprocity in the modified lattice is attributed to the synergy of nonlinearity (without it the localized NNM 21 cannot exist), scale hierarchy (with the localized NNM being spatially confined in the SS of the right-most cell) and asymmetry (of the linear coupling between cells).

We end this study by briefly revisiting the essentially nonlinear lattice considered in Secs. IIIA and IIIB. We found previously that in the absence of a linear component in the nonlinear coupling stiffnesses *reverse acoustic non-reciprocity* is realized, in the sense that standing wave localization occurs for *left* impulsive excitation and travelling wave propagation for *right* impulsive excitation. We wish to investigate briefly the cause of this "non-reciprocity reversal." In Fig. 20 we depict the FEP for the essentially nonlinear lattice

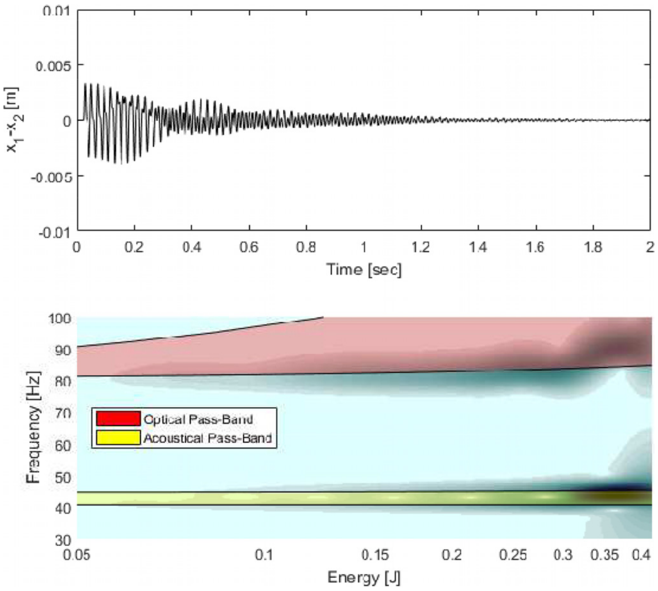

FIG. 19. (Color online) Relative responses between LS1 and SS1 of the modified lattice and the corresponding wavelet spectrum contour for left impulsive amplitude $F_0 = 350\,\mathrm{N}$; the wavelet spectrum is superimposed on the FEP of the underlying Hamiltonian system showing the nonlinear acoustical and optical passbands.

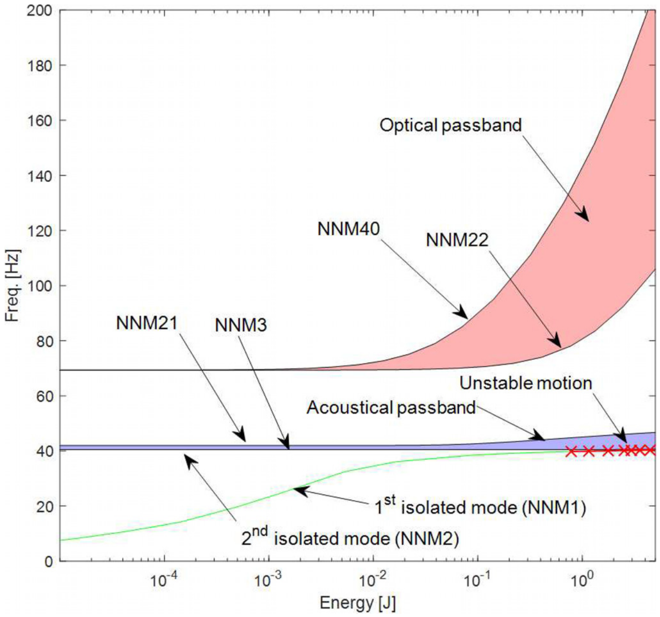

FIG. 20. (Color online) Frequency-energy plot (FEP) of the essentially nonlinear lattice with the two localized NNMs 1 and 2, the NNMs 3 and 21 approximately bounding the acoustical passband, and the NNMs 22 and 40 approximately bounding the optical passband (× denotes instability).

using the previous technique and notation, from which we deduce a qualitatively different picture regarding the location of the two isolated localized modes, which now are realized at low frequencies (NNMs 1 and 2 in Fig. 20), and are below the acoustic passband. Moreover, in this case the localized NNM 1 becomes unstable at high energies, a feature which was absent for the localized NNMs of the modified lattice. We now reconsider the spatiotemporal energy plots of Figs. 8(a) and 8(b) corresponding to points (p1) and (p2) of Fig. 9 for right impulsive excitation. In Fig. 21 we depict the corresponding relative responses between LS20 and SS20 in the last cell, together with their wavelet transform spectra superimposed on the FEP of Fig. 20. In addition, for comparison purposes in Fig. 22 we present similar depictions for the relative responses between LS1 and SS1 of the first cell for the same essentially nonlinear lattices but for left impulsive excitations with the same amplitudes. These results highlight the cause of non-reciprocity reversal in this case.

For right impulsive excitation [cf. Figs. 21(a) and 21(b)] the localized NNM of cell 20 is excited, but since this mode is located at low frequencies below the acoustical passband for low impulse amplitude [cf. Fig. 21(a)] and below the optical passband for high impulse amplitude [cf. Fig. 21(b)]. As a result, the amount of the applied energy localized at the right boundary is small, and the major part of this energy is transmitted into the lattice. This is evidenced by the harmonic components that are located in the two passbands, and especially the upper optical passband. A different situation occurs for left impulsive excitation [cf. Figs. 22(a) and 22(b)], where, irrespective of the amplitude of the applied impulse, there is no excitation of any localized NNM and the main harmonic components of the response are located in the lower acoustical passbands and there is negligible harmonic content in the upper optical passband. Given that breather formation in the lattice can only occur by excitation of the optical passband, and that excitation of the acoustical passband leads to weak wave transmission in the lattice, the net effect is energy localization close to its left boundary.

V. CONCLUDING REMARKS

The effect of on-site linear viscous damping on breather arrest, wave localization and acoustic non-reciprocity in elastically grounded, strongly nonlinear discrete semi-infinite and finite lattices was studied. As the first step, an impulsively forced simplified 2 DOF system composed of two linearly damped oscillators coupled through a purely

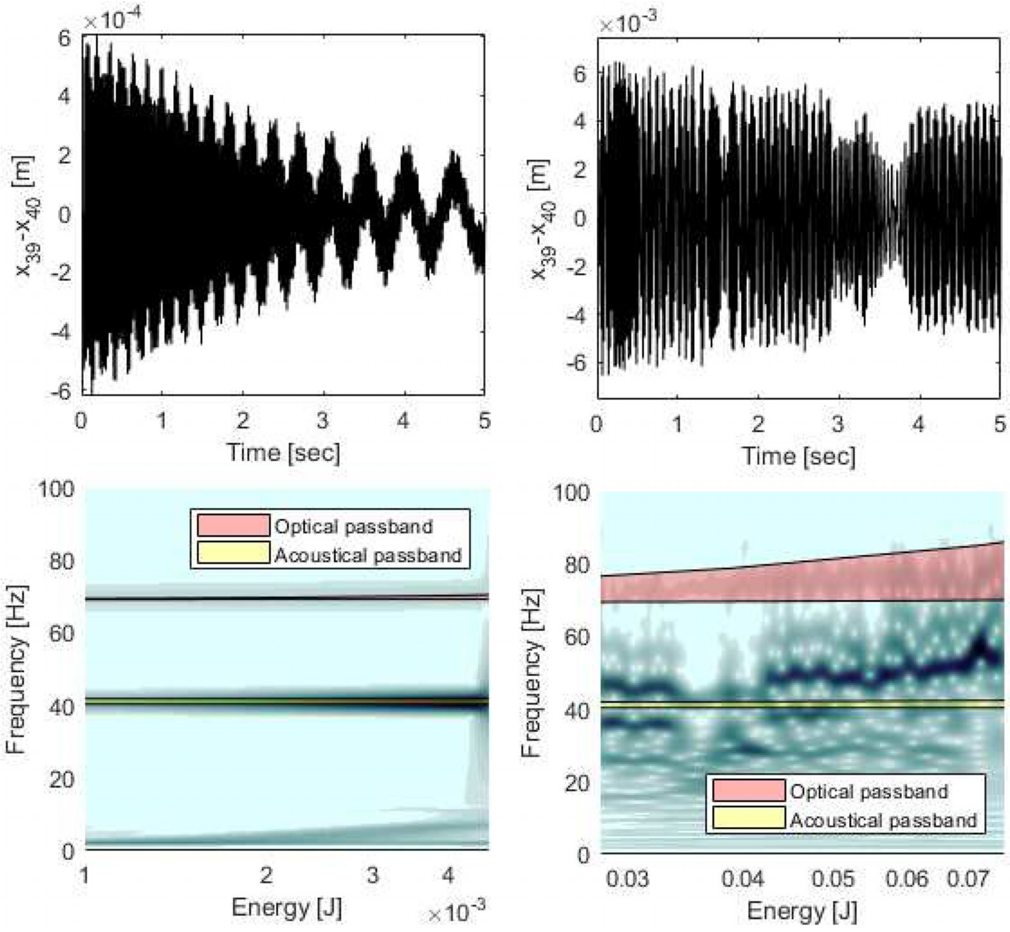

(a) (b)

FIG. 21. (Color online) Relative responses between LS20 and SS20 of the essentially nonlinear lattice and the corresponding contours of the wavelet spectra for right impulsive amplitude (a) $F_0 = 35\,\mathrm{N}$ and (b) $F_0 = 150\,\mathrm{N}$; the wavelet spectra are superimposed on the FEP of the underlying Hamiltonian system of Fig. 20 showing the nonlinear acoustical and optical passbands.

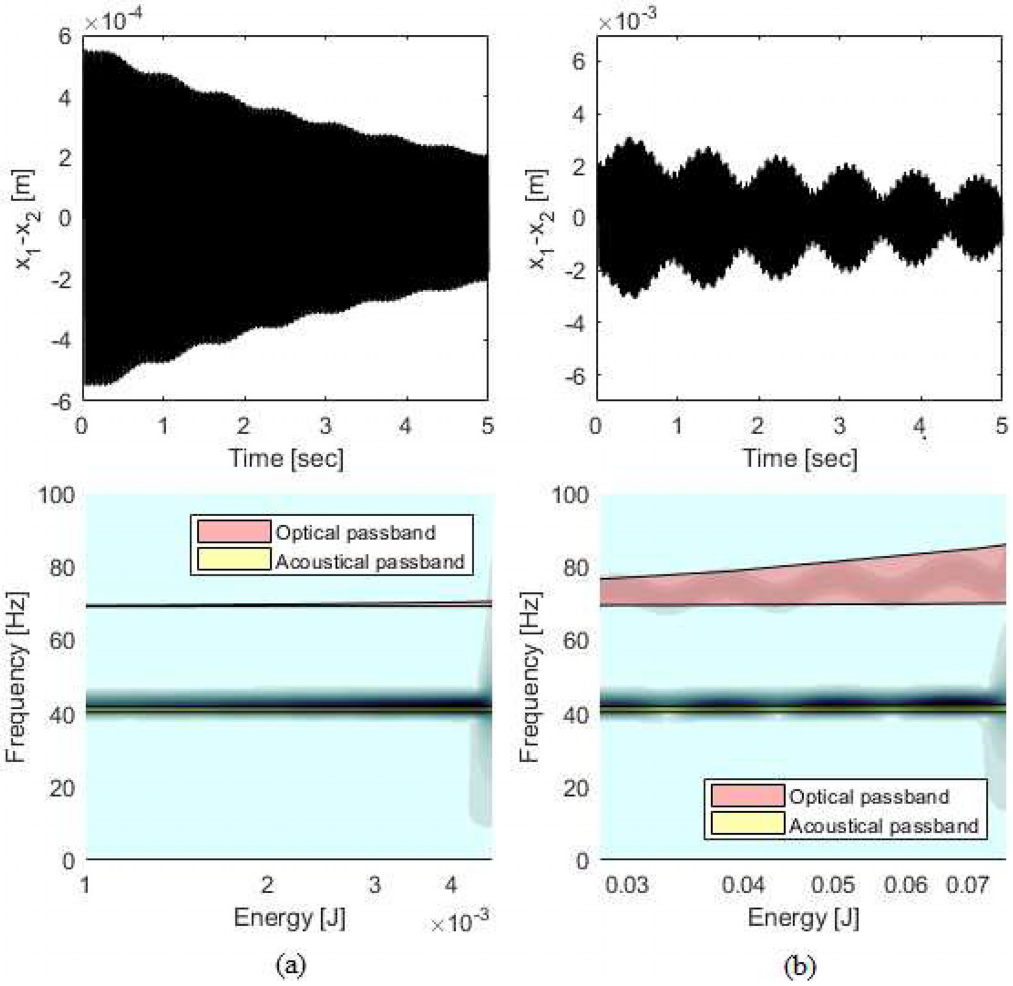

(a) (b)

FIG. 22. (Color online) Relative responses between LS1 and SS1 of the essentially nonlinear lattice and the corresponding contours of the wavelet spectra for left impulsive amplitude (a) $F_0 = 35\,\mathrm{N}$ and (b) $F_0 = 150\,\mathrm{N}$; the wavelet spectra are superimposed on the FEP of the underlying Hamiltonian system of Fig. 20 showing the nonlinear acoustical and optical passbands.

cubic nonlinear spring was studied, since this system admits approximate analytical solutions in the limit of small input energy. An interesting finding was that the finite number of nonlinear beats, i.e., of recurring energy exchanges, in this system was related to the damping coefficient and the initial impulse amplitude. Accordingly, we computed characteristic curves which related a specific maximum number of beats to the damping and forcing amplitudes (energy) required for their realization. In the next stage of the study a semi-infinite lattice of nonlinearly coupled damped oscillators and essential (pure) cubic nonlinearity was considered, as a semi-infinite extension of the simplified 2 DOF system. Impulsive excitation was applied to its free end, and the breather arrest phenomenon was demonstrated for varying damping coefficients and impulsive force amplitudes. Following this observation, breather penetration depth curves were computed, relating the amplitude of the impulsive force to the on-site damping coefficient for breather arrest at a specific particle of the lattice. It was found that similar power laws govern the breather penetration curves in the semi-infinite lattice and the characteristic curves for finite number of beats in the simplified system. Simply stated, it was shown that each breather depth penetration curve of the essentially nonlinear lattice is linearly proportional to a corresponding characteristic curve for finite beats of the simplified system. This strongly suggests that problems of breather arrest in nonlinear lattices can be studied and physically understood by considering appropriate simplified reduced-order models of coupled oscillators which are easier to analyze.

Motivated by the previous results, a more complicated system was considered, namely, a finite, strongly nonlinear, hierarchical and asymmetric lattice. This lattice was composed of a finite number of linearly coupled identical cells, with each cell composed of a linearly grounded large-scale particle (LS) that was nonlinearly coupled to an ungrounded small-scale particle (SS). Each SS of the lattice was coupled to the same cell-LS on its left through a strongly nonlinear cubic stiffness, while it was linearly coupled to the next cell-LS on its right. The arrangement of the linear coupling stiffnesses between cells resulted in an interesting asymmetry for the lattice, with the SS of the last (right-most) cell being "free" to oscillate, since it is only coupled on its left to the LS of the last cell. We considered two cases for the strongly nonlinear coupling stiffnesses of the lattices, i.e., either with essentially nonlinear stiffness characteristics or with linear components in their nonlinear stiffness characteristics. Perhaps some of the most interesting findings of this work are that (a) the asymmetry of the last SS is the main cause for acoustic non-reciprocity in this finite lattice, and is caused by a boundary effect; and (b) that the existence or absence of (even small) linear components in the nonlinear stiffnesses defines the main features of the non-reciprocal acoustics of the lattice, resulting either in breather formation and arrest on one end, and standing wave localization and absence of wave transmission on the other. Based on the absence or not of a small linear component in the nonlinear stiffnesses we distinguished between "essentially nonlinear" and "modified" lattices. The nonlinear mechanisms governing acoustic non-reciprocity, breather initiation and arrest and wave localization in both of these lattices were studied utilizing a simplified reduced-order model and by superimposing the wavelet spectra of the lattice responses on the frequency-energy plots (FEPs) of the corresponding Hamiltonian lattices. Breather initiation in the lattice was associated with harmonic components of the responses exciting the optical passband of the FEP, whereas standing wave localization and absence of wave transmission with either strong excitation of a localized NNM in the rightmost cell of the lattice and absence of excitation of the optical passband.

The results of this work underscore the strong influence of viscous damping and energy in the acoustics of nonlinear lattices, as well as the feasibility of studying and understanding complex nonlinear acoustical responses by studying appropriate reduced-order models that are easier to analyze. In addition, our results show the efficacy of relating the acoustics of nonlinear lattices to the FEPs of the corresponding underlying Hamiltonian lattices. Hence, the methods and results presented herein can be regarded as tools towards predictively designing strongly nonlinear lattices with desired non-reciprocity, localization, and breather arrest capacities.

ACKNOWLEDGMENTS

This work was supported in part by National Science Foundation Grant No. CMMI-17-1727761. Any opinion, findings, and conclusions or recommendations expressed in this work are those of the authors and do not necessarily reflect the views of the National Science Foundation.

APPENDIX: DERIVATION OF THE SECOND OF EXPRESSIONS (4)

Consider the second expression in Eq. (3),

$$w'' + w + \lambda w' + 2w^3 = 0, \tag{A1}$$

which can be expressed as

$$\begin{aligned} w' &= p, \\ p' &= -\lambda p - w - 2w^3. \end{aligned} \tag{A2}$$

For $|w| \ll 1$, the nonlinear term in Eq. (A2) can be approximately neglected, and this equation is approximately linear with action-angle variables of the corresponding undamped system given by

$$\begin{aligned} w &= \sqrt{2I}\sin\theta, \\ w' &= p = \sqrt{2I}\cos\theta. \end{aligned} \tag{A3}$$

Introducing this action-angle variable transformation into Eq. (A3) we express this system of equations as

$$\begin{aligned} I' &= -2I\lambda\cos^2\theta - 8I^2\sin^3\theta\cos\theta, \\ \theta' &= 1 + \lambda\sin\theta\cos\theta + 4I\sin^4\theta. \end{aligned} \tag{A4}$$

In the limit when $|w| \ll 1$ the first equation of Eq. (A4) can be averaged with respect to the fast angle θ yielding the following averaged equation:

$$J(\tau) = J_0\exp(-\lambda\tau), \tag{A5}$$

where $J = \langle I \rangle$ is the time-averaged action. Assuming weak viscous damping λ, the second equation in Eq. (A4) can also be averaged to obtain

$$\langle \theta' - 1 \rangle = \frac{3}{2}J_0\exp(-\lambda\tau). \tag{A6}$$

Assuming the initial condition $\theta(0+) = 0$, the solution of this averaged equation is expressed as

$$\theta(\tau) \approx \tau + \frac{3J_0}{2\lambda}\left[1 - \exp(-\lambda\tau)\right]. \tag{A7}$$

Denoting $N_0 = \sqrt{2J_0}$ while applying the initial conditions imposed on w, the approximate solution for w can be obtained as

$$w(\tau) \approx N_0\exp(-\lambda\tau/2)\sin\left\{\tau + \frac{3N_0^2}{4\lambda}[1 - \exp(-\lambda\tau)]\right\}. \tag{A8}$$

[1] R. S. MacKay, "Discrete breathers: Classical and quantum," Phys. A: Stat. Mech. Appl. **288**, 174–198 (2000).

[2] S. Aubry and T. Cretegny, "Mobility and reactivity of discrete breathers," arXiv:cond-mat/9712046 (1997).

[3] S. Flach and K. Kladko, "Moving discrete breathers?," Phys. D: Nonl. Phenom. **127**, 61–72 (1999).

[4] S. M. Robert and S. Jacques-Alexandre, "Effective Hamiltonian for travelling discrete breathers," J. Phys. A: Math. Gen. **35**, 3985 (2002).

[5] M. A. Hasan, Y. Starosvetsky, A. F. Vakakis, and L. I. Manevitch, "Nonlinear targeted energy transfer and macroscopic analog of the quantum Landau–Zener effect in coupled granular chains," Phys. D: Nonl. Phenom. **252**, 46–58 (2013).

[6] G. James, "Nonlinear waves in Newton's cradle and the discrete p-Schrödinger equation," Math. Models Meth. Appl. Sci. **21**, 2335–2377 (2011).

[7] Y. Zhang, K. J. Moore, D. M. McFarland, and A. F. Vakakis, "Targeted energy transfers and passive acoustic wave redirection in a two-dimensional granular network under periodic excitation," J. Appl. Phys. **118**, 234901 (2015).

[8] P. G. Kevrekidis, in *The Discrete Nonlinear Schrödinger Equation: Mathematical Analysis, Numerical Computations and Physical Perspectives* (Springer, Berlin, 2009), pp. 3–9.

[9] M. Toda, *Theory of Nonlinear Lattices* (Springer-Verlag, New York, 1989).

[10] M. Ablowitz and J. Ladik, "Nonlinear differential–difference equations and Fourier analysis," J. Math. Phys. **17**, 1011–1018 (1976).

[11] O. Bang and M. Peyrard, "High order breather solutions to a discrete nonlinear Klein-Gordon model," Phys. D: Nonl. Phenom. **81**, 9–22 (1995).

[12] G. James and Y. Sire, "Travelling breathers with exponentially small tails in a chain of nonlinear oscillators," Commun. Math. Phys. **257**, 51–85 (2005).

[13] Y. Sire and G. James, "Travelling breathers in Klein–Gordon chains," C. R. Math. **338**, 661–666 (2004).

[14] Y. Sire and G. James, "Numerical computation of travelling breathers in Klein–Gordon chains," Phys. D: Nonl. Phenom. **204**, 15–40 (2005).

[15] J. Bunyan, K. J. Moore, A. Mojahed, M. D. Fronk, M. Leamy, S. Tawfick, and A. F. Vakakis, "Acoustic nonreciprocity in a lattice incorporating nonlinearity, asymmetry, and internal scale hierarchy: Experimental study," Phys. Rev. E **97**, 052211 (2018).

[16] H. B. G. Casimir, "On Onsager's principle of microscopic reversibility," Rev. Mod. Phys. **17**, 343 (1945).

[17] L. Onsager, "Reciprocal relations in irreversible processes. II," Phys. Rev. **38**, 2265 (1931).

[18] L. Onsager, "Reciprocal relations in irreversible processes. I," Phys. Rev. **37**, 405 (1931).

[19] K. L. Tsakmakidis, L. Shen, S. A. Schulz, X. Zheng, J. Upham, X. Deng, H. Altug, A. F. Vakakis, and R. W. Boyd, "Breaking Lorentz reciprocity to overcome the time-bandwidth limit in physics and engineering," Science **356**, 1260–1264 (2017).

[20] B.-I. Popa and S. A. Cummer, "Non-reciprocal and highly nonlinear active acoustic metamaterials," Nat. Commun. **5**, 3398 (2014).

[21] S. A. Cummer, "Selecting the direction of sound transmission," Science **343**, 495–496 (2014).

[22] R. Fleury, D. L. Sounas, C. F. Sieck, M. R. Haberman, and A. Alù, "Sound isolation and giant linear nonreciprocity in a compact acoustic circulator," Science **343**, 516–519 (2014).

[23] R. Fleury, D. L. Sounas, and A. Alù, "Subwavelength ultrasonic circulator based on spatiotemporal modulation," Phys. Rev. B **91**, 174306 (2015).

[24] B. Liang, X. S. Guo, J. Tu, D. Zhang, and J. C. Cheng, "An acoustic rectifier," Nat. Mater. **9**, 989–992 (2010).

[25] N. Boechler, G. Theocharis, and C. Daraio, "Bifurcation-based acoustic switching and rectification," Nat. Mater. **10**, 665–668 (2011).

[26] J. Zhang, B. Peng, Ş. K. Özdemir, Y.-x. Liu, H. Jing, X.-y. Lü, Y.-l. Liu, L. Yang, and F. Nori, "Giant nonlinearity via breaking parity-time symmetry: A route to low-threshold phonon diodes," Phys. Rev. B **92**, 115407 (2015).

[27] F. Li, P. Anzel, J. Yang, P. G. Kevrekidis, and C. Daraio, "Granular acoustic switches and logic elements," Nat. Commun. **5**, 5311 (2014).

[28] M. Maldovan, "Sound and heat revolutions in phononics," Nature **503**, 209–217 (2013).

[29] D. E. Panayotoukanos, N. D. Panayotounakou, and A. F. Vakakis, "On the solution of the unforced damped duffing oscillator with no linear stiffness term," Nonl. Dyn. **28**, 1–16 (2002).

[30] M. D. Fronk, S. Tawfick, C. Daraio, A. F. Vakakis, and M. J. Leamy, "Non-reciprocity in structures with nonlinear internal hierarchy and asymmetry," V008T12A023 (2017).

[31] K. J. Moore, J. Bunyan, S. Tawfick, O. V. Gendelman, S. Li, M. Leamy, and A. F. Vakakis, "Nonreciprocity in the dynamics of coupled oscillators with nonlinearity, asymmetry, and scale hierarchy," Phys. Rev. E **97**, 012219 (2018).

[32] A. F. Vakakis, O. V. Gendelman, L. A. Bergman, D. M. McFarland, G. Kerschen, and Y. S. Lee, *Nonlinear Targeted Energy Transfer in Mechanical and Structural Systems* (Springer, Dordrecht, the Netherlands, 2008).

[33] G. Kerschen, M. Peeters, J. C. Golinval, and A. F. Vakakis, "Nonlinear normal modes, Part I: A useful framework for the structural dynamicist," Mech. Syst. Sign. Process. **23**, 170–194 (2009).

[34] M. Peeters, R. Viguié, G. Sérandour, G. Kerschen, and J. C. Golinval, "Nonlinear normal modes, Part II: Toward a practical computation using numerical continuation techniques," Mech. Syst. Sign. Process. **23**, 195–216 (2009).

[35] K. R. Jayaprakash, Y. Starosvetsky, A. F. Vakakis, M. Peeters, and G. Kerschen, "Nonlinear normal modes and band zones in granular chains with no pre-compression," Nonl. Dyn. **63**, 359–385 (2011).